Remote Sensing of Environment 120 (2012) 197–207

Contents lists available at SciVerse ScienceDirect

Remote Sensing of Environment

journal homepage: www.elsevier.com/locate/rse

Simulation of Sentinel-3 images by four-stream surface–atmosphere radiative transfer modeling in the optical and thermal domains

Wout Verhoef [a,*], Heike Bach [b]

[a] Faculty of Geo-Information Science and Earth Observation (ITC), University of Twente, P.O. Box 217, 7500 AE Enschede, The Netherlands
[b] Vista GmbH, Gabelsbergerstraβe 51, 80333 Munich, Germany

ARTICLE INFO

Article history:
Received 22 December 2010
Received in revised form 21 September 2011
Accepted 19 October 2011
Available online 15 February 2012

Keywords:
Top-of-atmosphere
Image simulation
Radiative transfer
Sentinel-3
Optical
Thermal
SLC
MODTRAN

ABSTRACT

Simulation of future satellite images can be applied in order to validate the general mission concept and to test the performance of advanced multi-sensor algorithms for the retrieval of surface parameters. This paper describes the radiative transfer modeling part of a so-called Land Scene Generator (LSG) that was developed to simulate images of the sensors OLCI (Ocean and Land Colour Instrument) and SLSTR (Sea and Land Surface Temperature Radiometer) on board of the Sentinel-3 mission. Features of this mission are its wide spectral coverage (optical and thermal domains) and its wide imaging swath, which imposes particular requirements on the simulator in dealing with atmospheric effects over both spectral domains and with angular effects caused by variations in surface bi-directional reflectance distribution function (BRDF) and atmospheric scattering. In the simulator, radiative transfer models for the combination vegetation-soil and for water are coupled to atmospheric parameters derived from MODTRAN runs in order to calculate top-of-atmosphere radiances. For this, four-stream radiative transfer theory is applied to allow simulation of BRDF effects, topography effects, adjacency effects, as well as its uniform application over the optical and thermal spectral domains.

1. Introduction

Simulation of terrestrial scenes mostly has been applied for 3D-scenes at very high spatial detail of the order of cm to dm. For urban areas this was demonstrated by Poglio et al. (2006). The Discrete Anisotropic Radiative Transfer (DART) model, developed at the Centre d'Études Spatiales de la Biosphère (CESBIO), (Gascon et al., 2001; Gastellu-Etchegorry et al., 2004) is a prominent example of a ray-tracing method to simulate realistic complex 3-D scenes, i.e. urban and/or natural Earth landscapes, possibly with topography effects and including the atmosphere. DART allows simulations from the visible to the thermal infrared domains (0.3–15 μm). Much work has also been done in the area of SAR image simulation, which is however not comparable with methods for optical sensors.

Land scene simulations of a hyperspectral sensor at a lower spatial resolution of ~50 m have been performed in studies under ESA contract (Verhoef & Bach, 2003, 2007), like the studies in preparation of the SPECTRA candidate Earth Explorer mission, which was later canceled. In that case the simulations particularly addressed the hyperspectral aspect (200 bands) and the multi-angular image acquisition (7 along-track directions) of that mission (Verhoef & Bach, 2003). Within-scene variations of the sun-target-sensor angular geometry were only modest for SPECTRA. These aspects, extension over the entire optical – thermal domain and wide-swath imagery, do play a prominent role in a scene generator developed for Sentinel-3 and will be discussed in the following sections.

One can follow several approaches for the simulation of remote sensing images. The first is based on applying look-up tables to land-use classified image data. However, in this case within-class texture variations are ignored, and within-scene variations of the sun-target-sensor angular geometry are ignored as well, since these would require angle-dependent look-up tables, which are hard to define without a model approach. An alternative approach is based on using existing remote sensing data and reconditioning these as much as possible to adjust them to the properties of the sensor to be simulated. This however involves the use of spectral and angular interpolations and extrapolations. Examples of this are using airborne data, that can of course not be representative for wide-swath acquisitions over large areas. Additionally it is not justified to simply interpolate spectral reflectance signatures, or resample new spectra from broad spectral bands, since absorption features are very wavelength dependent and any polynomial interpolation that does not take these features into account must fail. Therefore, an approach based on radiative transfer modeling was chosen, in which the required spatial information on surface properties, that varies pixel by pixel, and which is called texture information in the following, is extracted from satellite data. This texture information must include the most significant optical properties of the land surface. Most important is

* Corresponding author. Tel.: +31 53 4874289; fax: +31 53 4874336.
E-mail addresses: verhoef@itc.nl (W. Verhoef), bach@vista-geo.de (H. Bach).

0034-4257/$ – see front matter © 2012 Elsevier Inc. All rights reserved.
doi:10.1016/j.rse.2011.10.034

the land surface class the pixel belongs to (water, snow, open soil, forest, other vegetation). This classification allows the assignment of the relevant optical mechanisms to be considered in the radiative transfer calculations (e.g. for water the impact of the water constituents chlorophyll and sediments have to be modeled; for vegetated areas the canopy reflectance and the contribution of leaves are required; for forest additional structural effects like crown cover and their shading need to be considered and for open soil the impact of soil moisture has to be simulated in an adequate way). The amount of vegetation, which can be parameterized with the leaf area index, is spectrally the most influential parameter for any vegetated pixel and for open soil the surface moisture is determining the reflectance properties most. This explains that the "textural" information layers refer to bio-, geophysical variables of the land surface in the presented Sentinel-3 simulations. As satellite data source that provided these textural information layers Landsat imagery was selected, since the Thematic Mapper sensor has an adequate spatial resolution and sufficient spectral coverage to allow model inversion in terms of biophysical parameters for several land use classes. These textural parameter fields can next be used in a forward model simulating TOA radiances for the associate angular geometry, spectral coverage and spatial resolution of the Sentinel-3 instruments.

The SLSTR (Sea and Land Surface Temperature Radiometer) sensor on board of Sentinel-3 will have spectral bands in the region from the visible to the thermal infrared parts of the spectrum, and one in the optical-thermal transition region at 3.74 μm, where optical and thermal effects are equally important. It uses conical scanning mechanisms to generate a near-nadir looking image as well as a backward looking image under a constant viewing zenith angle of 55°. The OLCI (Ocean and Land Colour Instrument) sensor is a push-broom scanner with a cross-track field of view of 68.5° and covers the spectral range from 380 to 1050 nm in 23 bands of widths varying from 2.5 to 40 nm.

This paper deals with a limited number of aspects that have played a role in the design of the simulator for Sentinel-3. Section 2 discusses the radiative transfer models applied, and the angular geometry aspects for the given instruments. In Section 3 the main aspects related to image modeling in practice for this particular application are discussed, such as the surface–atmosphere interaction over the solar-reflective and thermal domains of the spectrum, the extraction of atmospheric parameters by the MODTRAN interrogation technique (MIT), the angular interpolation methodology applied, and the modeling of the spectral properties of the sensors SLSTR and OLCI. In Section 4 some examples of modeling outputs are shown, and Section 5 discusses how simulated images can be used in a multi-sensor data assimilation approach. Aspects not covered in this contribution are more sensor-specific, like the instrument's point spread functions, signal-to-noise performance, phenomena like smile (a shifting of the spectral calibration depending on the spatial position within the swath), et cetera.

2. Radiative transfer models

In order to simulate imagery over land one has to use a combination of radiative transfer models representing different categories of surface objects and the atmosphere. In the Sentinel-3 Land Scene Generator the coupled model SLC (soil-leaf-canopy) is used to model the spectral responses of various vegetation–soil combinations. The optical water quality model WASI (Gege, 2004, 2005) is used to simulate the reflectance of in-land water bodies. The atmospheric radiative transfer model MODTRAN4 (Berk et al., 1999) is applied to simulate the atmospheric effects. Finally, four-stream radiative transfer (Verhoef & Bach, 2007) is applied to describe the coupling between the atmosphere and the non-Lambertian surface and to derive top-of-atmosphere spectral radiances in the optical and thermal domains. The mentioned models are described in some more detail in the next sections.

2.1. Soil–leaf–canopy (SLC) model

For the simulation of wide-swath remote sensing images with their associated geographic extent, such as required for simulation of the Sentinel-3 sensors OLCI and SLSTR, one needs a model that is fairly realistic but also has a high processing throughput. The SLC model (Verhoef & Bach, 2007) fulfills these requirements. Its canopy sub model 4SAIL2 has successfully participated in the RAMI-3 model comparison exercise (Widlowski et al., 2007), where for the so-called "floating spheres" experiment it showed nearly the same performance as much more sophisticated 3D ray-tracing models. SLC however has the advantage that it is faster and simpler to apply. This is a prerequisite for parameter retrieval using model inversion. Thus, SLC can first be applied for the retrieval of the pixel-by-pixel textural properties of a scene (model inversion stage), and later be applied again to simulate images under arbitrary observation conditions (possibly including the atmosphere and sensor properties). The latter is the forward modeling stage. SLC, as an extension of 4SAIL2, allows the simulation of the BRDF properties of the land surface from biophysical parameters (e.g. leaf area, leaf angle distribution, chlorophyll content). It thus allows the realistic simulation of the spectral and angular "behavior" of Sentinel-3 data. The land surface reflectance model to be used for the scene texture generation is thus the model SLC. This coupled model is fully integrated and consists of the following sub-models:

- 4SOIL, a modified Hapke model (Hapke, 1981; Pinty et al., 1989) for simulation of soil BRDF effects
- Spectral soil moisture effect model (Bach & Mauser, 1994)
- PROSPECT leaf optical properties model (Jacquemoud & Baret, 1990)
- 4SAIL2, a two-layer version of SAIL (Verhoef, 1984, 1998) including crown clumping

These four modeling components above have been integrated in a Windows DLL which can be called from several environments. Successful demo implementations have been realized with the languages Visual Basic 5 and Java.

The inputs of SLC are shown in Fig. 1, which also illustrates the so-called four-stream concept of radiative transfer modeling. Table 1 gives a more detailed description of all input parameters of the model.

The two-layer structure of the canopy model 4SAIL2 is illustrated in Fig. 2, which shows that two parameters are used to describe a vertical leaf color gradient, namely the fraction brown leaf area f_B and a dissociation factor D. For D equal to unity, dissociation is complete, which means that all green leaves are in the top layer and all brown leaves in the bottom layer. For D equal to zero, all leaves are homogeneously mixed over the two layers, and effectively this means that there is only one homogeneous layer. The effect of crown clumping is illustrated in Fig. 3. Here also two parameters are used to describe this effect, namely the vertical crown coverage Cv (the fraction of crown area as observed from above) and a tree shadow-factor zeta, which is equal to the ratio of crown diameter to crown height. For Cv equal to one, the canopy becomes laterally homogeneous and in that case the tree shadow-factor has no effect. If Cv is less than zero, then one can identify four area fractions on the ground surface, namely the area fraction that is visible from above and that is in the sun (Fos), visible area that is in the shade of tree crowns (Fod), obscured area in the sun (Fcs) and finally obscured area in the shade (Fcd). These are illustrated in Fig. 3 for the simplified case of a single tree crown that is observed from above and of which the shadow is shifted with respect to the vertical projection of the crown. It is assumed that

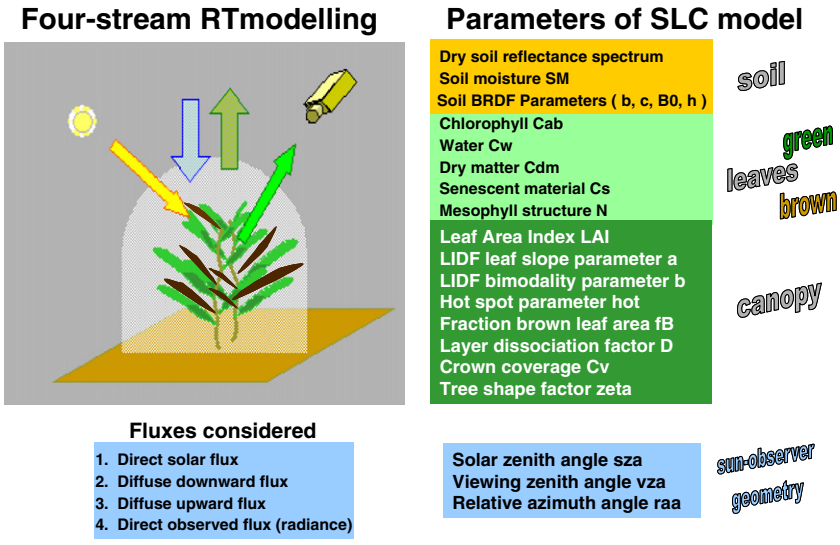

Fig. 1. Four-stream modeling concept and the inputs of the SLC model.

there can be several crowns in a single pixel, so the shadowing effects are only considered in statistical terms.

The sum of the four fractions always equals one, but their relative proportions are important for the reflectance of the combination tree crowns – background.

The four more important canopy structure parameters, also known from earlier versions of SAIL, are mentioned in Fig. 1 and these are the LAI (leaf area index), the LIDF (leaf inclination distribution function) parameters *a* and *b*, and finally the hot spot parameter.

2.2. Water model WASI

Water simulations are not a central component of the LSG, since it concentrates on the land surface. However since water bodies are always part of the land surface and also coastal areas may be simulated, an approach is required that provides reflectance values for water surfaces. Accordingly a simplified water reflectance model was developed that uses model outputs from the WASI model (Water Color Simulator) developed at DLR (Gege, 2004, 2005).

The textural parameters selected to allow the spatial variation of the water reflectance are the content of suspended matter and the phytoplankton concentration, since these two factors dominate the scattering and absorption processes in water.

The WASI model is applied for a set of predefined values of suspended matter and phytoplankton. As output "remote sensing reflectance above surface for deep water" was selected in WASI. Suspended matter for large particles is varied from 0.1 to 50 mg/l in 10 intervals. The phytoplankton content is tabulated for a low (3 µg/l) and high (40 µg/l) concentration. The WASI model outputs for these values of suspended matter and phytoplankton are illustrated in Fig. 4.

If a water pixel is simulated in the LSG, first the suspended matter and phytoplankton contents of this pixel are retrieved from the texture file. Then the reflectance spectra are interpolated for these values from the tabulated data using a two-dimensional non-linear interpolation technique. In a first step using the texture information on suspended matter, the water reflectance is linearly interpolated from the closest suspended matter spectra in the look up table. This is done for the low and high phytoplankton case. The resulting spectra for 2 sets of phytoplankton contents (3 and 40 µg/l) are again inter- or extrapolated using the phytoplankton values from the texture information of the pixel under consideration. Since the absorption of the phytoplankton follows an exponential law, in this second step the

Table 1
Input parameters of the SLC model.

Parameter	Description	Unit
Hapke_b	Hapke phase function parameter b	–
Hapke_c	Hapke phase function parameter c	–
Hapke_h	Hapke hot spot width parameter	–
Hapke_B0	Hapke hot spot magnitude parameter	–
SM%	Soil moisture percentage	–
Cab_green	Chlorophyll content green leaves	µg/cm^2
Cw_green	Water content green leaves	g/cm^2
Cdm_green	Dry matter content green leaves	g/cm^2
Cs_green	Brown pigment content green leaves	–
N_green	Mesophyll structure parameter green leaves	–
Cab_brown	Chlorophyll content brown leaves	µg/cm^2
Cw_brown	Water content brown leaves	g/cm^2
Cdm_brown	Dry matter content brown leaves	g/cm^2
Cs_brown	Brown pigment content brown leaves	–
N_brown	Mesophyll structure parameter brown leaves	–
LAI	Total leaf area index (per crown)	m²/m²
LIDFa	LIDF parameter a	–
LIDFb	LIDF parameter b	–
hot	Hot spot parameter	–
fB	Fraction brown leaf area	–
D	Layer dissociation factor	–
Cv	Vertical crown cover fraction	–
zeta	Tree shadow factor	–
sza	Solar zenith angle	deg
vza	Viewing zenith angle	deg
raa	Relative azimuth angle	deg

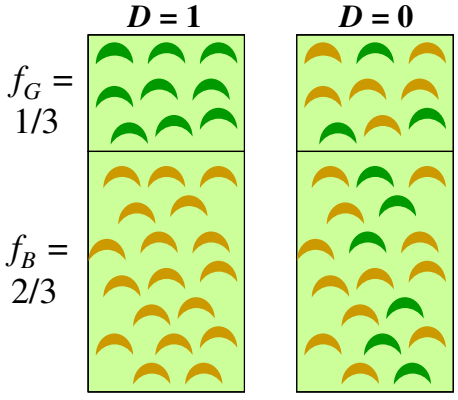

Fig. 2. Leaf color gradients in two-layer model for extreme values of the dissociation factor D.

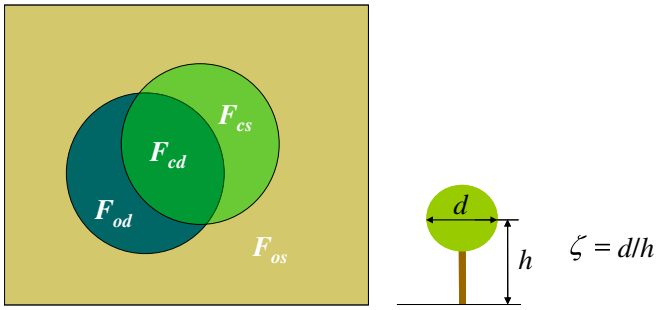

Fig. 3. Ground area fractions controlling the effect of crown clumping (left) and illustration of the tree shape factor (right).

logarithmic phytoplankton values are used in the linear interpolation or extrapolation.

Valid ranges of the texture information for this simplified water reflectance model were selected according to the applied LUT. They are allowed to vary between 1 to 60 μg/l for phytoplankton and 0.1 to 70 mg/l for suspended matter. If the texture file provides concentrations of phytoplankton and suspended matter in these ranges, realistic water reflectances can thus be calculated using the simplified water reflectance model.

2.3. Atmospheric model MODTRAN4

The atmospheric radiative transfer model MODTRAN (Berk et al., 1999) represents the state of the art for practical applications of atmospheric correction and forward simulation in remote sensing studies over a wide spectral range at a high spectral resolution. In the context of the Land Scene Generator the model has been applied to generate look-up tables of atmospheric parameters over a large number of wavelengths covering the spectral bands of the involved sensors OLCI and SLSTR. In the look-up tables generated the MODTRAN parameter Visibility was varied over 5 states, the atmospheric profile also over 5 states, and the sun-target-sensor angular geometry (the angles vza, sza, raa) over $12\times15\times5=900$ states. The angular interpolation method that is applied in the simulator is further described in Section 3.4.

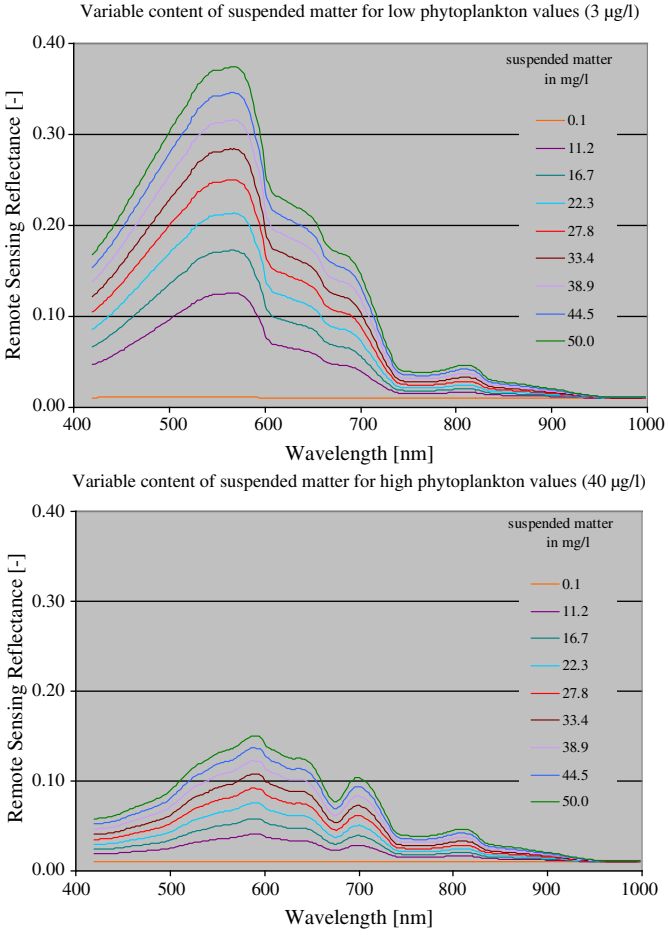

Fig. 4. WASI model outputs used in the simplified water reflectance model for variable suspended matter content and a low (top) and high (bottom) phytoplankton content.

2.4. Sun-target-sensor angular geometry modeling

Variations of the angular sun-target-sensor geometry over an image are modeled outside of the LSG. This means that the simulator is not exclusively related to the sensors OLCI and SLSTR, but that in principle it can handle any wide-swath sensor, provided the associated angles (solar zenith angle, solar azimuth, viewing zenith angle, viewing azimuth) are given as input on a pixel-by-pixel basis. This is done by providing to the simulator not only the texture layers describing the object properties, but also the four angles describing the local sun-target-sensor geometry.

2.5. Summary of input variables in the scene simulation

Besides the angular and solar geometry, the other textural information required layers for the scene simulations which are summarized in Table 2. Most describe land surface properties, except the last one, which provides a spatially distributed atmospheric property. The units and valid ranges of each texture info item are also listed in Table 2. If the textural layer of a pixel has an indicator for "missing value", which stands for not applicable, this texture layer is assigned according to a tabulated standard value for the respective land use code.

3. Modeling aspects

3.1. Four-stream surface–atmosphere coupling

The coupling between a non-Lambertian surface and the atmosphere has been described before by means of four-stream radiative transfer theory in Verhoef and Bach (2003, 2007). In the context of the LSG simulator, two elements have since been added, (i) the incorporation of thermal radiation, and (ii) the topography effect. For low to medium spatial resolution sensors like SLSTR and OLCI the adjacency effect is of less importance than for high resolution sensors, so spatial filtering of the upward hemispherical flux at the surface was not considered necessary in this case. Eqs. (1) and (2) describe all relevant interactions amongst the spectral radiative fluxes in the atmosphere and at the surface, including thermal radiation and topography effects:

$$E_s(b) = \tau_{ss} E_s(t) \tag{1a}$$

$$E^-(b) = \tau_{sd} E_s(t) + \rho_{dd} E^+(b) + \pi L_a(b) \tag{1b}$$

$$E_o(t) = \rho_{so} E_s(t) + \tau_{do} E^+(b) + \tau_{oo} E_o(b) + \pi L_a(t) \tag{1c}$$

$$E^+(b) = r_{sd} E_s(b) + r_{dd} E^-(b) + (1-r_{dd})\pi L_s \tag{2a}$$

$$E_o(b) = r_{so} V_{sun} E_s(b) + r_{do} V_{sky} E^-(b) + (1-r_{do})\pi L_s \tag{2b}$$

The physical quantities used in Eqs. (1) and (2) are explained in Table 3. Eqs. (1c) and (2b) describe the interactions involved in the generation of radiance in the observer's direction, L_o. The quantity

Table 2
List of textural spatial information layers and their specifications.

Information content	Unit	Valid ranges	Applicability to categories agri (A), forest (F) and water bodies (W)
Landuse code	–	NA	AF; with all SLC parameters tabulated for each landuse code
Soil/background code	–	NA	AF; spectral single scattering albedo values for each soil or background tabulated
Soil moisture	–	0.05–0.70	A
Leaf area index	m^2/m^2	0.0–9.0	AF
Fraction of brown leaves	–	0.0–1.0	AF
Crown cover	–	0.0–1.0	F
Leaf chlorophyll content	$\mu g/cm^2$	0.0–100.0	AF
Leaf dry matter content	g/cm^2	0.02–0.04	F
Phytoplankton content	µg/l	0.0–100.0	W
Suspended matter	mg/l	0.0–70.0	W
Surface radiometric temperature	K	240.0–340.0	AWF
Atmospheric visibility	km	5–80	AWF

used in these equations is π times this radiance, with symbol E_o, and is called flux-equivalent radiance, since it is the flux density that would result if the radiance would be isotropic and equal to L_o in all upward directions. The arguments (b) and (t) attached to the fluxes (except L_s) refer to the bottom and the top of the atmosphere, respectively. For surface reflectances the symbol r is used, for reflectances caused by volume scattering in the atmosphere we use the symbol ρ, and for atmospheric transmittances the symbol τ. Each of these quantities has double subscripts indicating the types of incident radiation and exiting radiation, where s stands for direct solar radiation, d for diffuse upward or downward flux and o for radiance in the observer's direction.

The viewing factors related to the local topography effect are given by

$$V_{\mathrm{sun}} = \cos\theta_t + \tan\theta_s \sin\theta_t \cos(\varphi_s - \varphi_t)$$

$$V_{\mathrm{sky}} = \frac{1+\cos\theta_t}{2}$$

where θ_t is the terrain slope inclination, θ_s is the solar zenith angle, φ_t is terrain slope azimuth, and φ_s the solar azimuth angle. They express how the irradiances from the sun and the sky are changed by the local slope and azimuth angle. Although the effects of terrain slope and aspect angle can be modeled in this way, it must be emphasized that in this approach within-pixel variations of these angles are not considered and that possible changes in the surface BRDF related to terrain topography are ignored as well.

Eqs. (1) and (2) in principle refer to monochromatic radiation, but they are general enough to describe solar reflective and thermal effects simultaneously, so that they apply also to the transition region from 3 to 5 µm, where both can play significant roles. Solution of Eqs. (1) and (2) is accomplished by first solving the diffuse fluxes at the bottom-of-atmosphere level. This can be done by combining Eqs. (1b) and (2a). For this, the thermal radiances $L_a(t)$, $L_a(b)$ and L_s are assumed to be known. Also, the solar irradiance at the top of the atmosphere $E_s(t)$ has to be known. This quantity is usually expressed in the so-called extra-terrestrial irradiance E_s^o, by the equation $E_s(t) = E_s^o \cos\theta_s$, where θ_s is the local solar zenith angle. After solving the diffuse fluxes $E^-(b)$ and $E^+(b)$, they are next substituted into Eqs. (2b) and (1c) to obtain $E_o(t)$, which is π times the top-of-atmosphere (TOA) radiance detected by a sensor.

The final result in terms of TOA radiance can be expressed by

$$\begin{aligned} L_{\mathrm{TOA}} = {} & L_{\mathrm{P0}} + L_a(t) \\ & + \frac{G_{\mathrm{ssdo}} r_{\mathrm{sd}} + G_{\mathrm{sddo}} r_{\mathrm{dd}} + L_a(b) r_{\mathrm{dd}} \tau_{\mathrm{do}} + (1-r_{\mathrm{dd}}) L_s \tau_{\mathrm{do}}}{1-r_{\mathrm{dd}}\rho_{\mathrm{dd}}} \\ & + \frac{G_{\mathrm{sdoo}} + G_{\mathrm{mult}} r_{\mathrm{sd}} + L_a(b)\tau_{\mathrm{oo}} + (1-r_{\mathrm{dd}}) L_s \rho_{\mathrm{dd}} \tau_{\mathrm{oo}}}{1-r_{\mathrm{dd}}\rho_{\mathrm{dd}}} V_{\mathrm{sky}} r_{\mathrm{do}} \\ & + V_{\mathrm{sun}} G_{\mathrm{ssoo}} r_{\mathrm{so}} + (1-r_{\mathrm{do}}) L_s \tau_{\mathrm{oo}} \end{aligned} \tag{3}$$

where the four successive lines on the right-hand side can be identified as the contributions related to (1) target-independent atmospheric path radiance, (2) adjacency effects, (3) directly reflected sky illumination on the target, and (4) directly reflected solar illumination and directional thermal emittance from the target. In Eq. (3) spectrally variable constants have been defined as:

$$L_{\mathrm{P0}} = \frac{E_s^o \cos\theta_s}{\pi} \rho_{\mathrm{so}}$$

$$G_{\mathrm{ssoo}} = \frac{E_s^o \cos\theta_s}{\pi} \tau_{\mathrm{ss}} \tau_{\mathrm{oo}}$$

$$G_{\mathrm{ssdo}} = \frac{E_s^o \cos\theta_s}{\pi} \tau_{\mathrm{ss}} \tau_{\mathrm{do}}$$

$$G_{\mathrm{mult}} = \frac{E_s^o \cos\theta_s}{\pi} \tau_{\mathrm{ss}} \rho_{\mathrm{dd}} \tau_{\mathrm{oo}}$$

$$G_{\mathrm{sddo}} = \frac{E_s^o \cos\theta_s}{\pi} \tau_{\mathrm{sd}} \tau_{\mathrm{do}}$$

$$G_{\mathrm{sdoo}} = \frac{E_s^o \cos\theta_s}{\pi} \tau_{\mathrm{sd}} \tau_{\mathrm{oo}}$$

Each G-term expresses a certain 'gain' factor that can be applied to convert a given surface reflectance component into a corresponding TOA radiance contribution, and therefore their units are also radiance units.

Eq. (3) includes solar reflective contributions on the left of each term, as well as thermal emission terms on the right side. The term describing the multiple reflections between the surface and the atmosphere, and which is equal to the infinite geometrical series $1 + r_{\mathrm{dd}}\rho_{\mathrm{dd}} + (r_{\mathrm{dd}}\rho_{\mathrm{dd}})^2 + ... = 1/(1 - r_{\mathrm{dd}}\rho_{\mathrm{dd}})$, has always been left intact to preserve consistency throughout the spectrum, although in

Table 3
Physical quantities involved in surface–atmosphere radiative transfer interactions. All quantities except the viewing factors are of a spectral nature.

E_s	Direct solar irradiance on a horizontal plane (SI unit $Wm^{-2}\,\mu m^{-1}$)
E^-	Downward diffuse irradiance (SI unit $Wm^{-2}\,\mu m^{-1}$)
E^+	Upward diffuse irradiance (SI unit $Wm^{-2}\,\mu m^{-1}$)
E_o	Radiance in the observer's direction, times π (SI unit $Wm^{-2}\,sr^{-1}\,\mu m^{-1}$)
L_a	Thermal emitted radiance by the atmosphere (SI unit $Wm^{-2}\,sr^{-1}\,\mu m^{-1}$)
L_s	Thermal emitted black body radiance from the surface (unit $Wm^{-2}\,sr^{-1}\,\mu m^{-1}$)
τ_{ss}	Direct transmittance of solar radiation
τ_{oo}	Direct transmittance in the direction of observation
τ_{sd}	Diffuse transmittance of solar radiation
τ_{do}	Diffuse transmittance in the direction of observation
ρ_{so}	Bidirectional reflectance at the top of the atmosphere (for a black earth surface)
ρ_{dd}	Bi-hemispherical reflectance at the bottom of the atmosphere (spherical albedo)
r_{so}	Surface bidirectional reflectance
r_{do}	Surface hemispherical–directional reflectance
r_{sd}	Surface directional–hemispherical reflectance
r_{dd}	Surface bi-hemispherical reflectance
V_{sun}	Topography effect viewing factor for solar radiation
V_{sky}	Topography effect viewing factor for diffuse incident radiation

the thermal domain it can probably be very well approximated by unity.

The term L_s in Eq. (3) represents the thermal surface blackbody radiance at the given wavelength, and is obtained by extracting from the texture layer the absolute surface temperatures T, and next applying the Planck function given by

$$L_s = \frac{c_1\left(\lambda \times 10^{-6}\right)^{-5}}{\exp\left(\frac{c_2}{\lambda T}\right)-1}$$

where λ is given in μm, and the constants are

$$c_1 = 1.191066 \times 10^{-22}\ \mathrm{W m^3\ \mu m^{-1} sr^{-1}}$$
$$c_2 = 14388.33\ \mathrm{\mu m K}$$

Note, that this gives only the blackbody radiances. In Eq. (3) this blackbody radiance is multiplied by the factor $(1-r_{do})$ to take into the account the directional emissivity of the surface. Thus the so-called blackbody radiance L_s in units of $\mathrm{W m^{-2} \mu m^{-1} sr^{-1}}$ is calculated from surface temperature. Surface temperatures can be obtained from a Landsat Thematic Mapper image (band 6) by applying the inverse Planck function (with surface emissivity correction). Next, the forward Planck function and an assumed or modeled (wavelength–dependent) surface emissivity can be used to predict the emitted surface radiance at other thermal wavelengths to simulate thermal imagery for other sensors.

3.2. MODTRAN interrogation technique

The MODTRAN interrogation technique (MIT) is a method (Verhoef & Bach, 2003) to extract relevant atmospheric parameters from three MODTRAN runs. The MIT method, which formerly was only limited to the solar-reflective domain, has been extended and unified to include also the thermal domain. It was found that all required atmospheric parameters can still be obtained from the responses of three MODTRAN "interrogations", made for surface albedos of 0.0, 0.5 and 1.0, identical to the former set-up. With a four-stream model of the surface–atmosphere interaction including the thermal domain, describing the MODTRAN runs for a uniform Lambertian surface reflectance with a spectrally flat albedo a (and emissivity $1-a$), the TOA radiance signal can be decomposed into the following contributions:

$$\begin{aligned} L_{TOA} = &\left[\rho_{so} + \frac{(\tau_{ss}+\tau_{sd})a(\tau_{do}+\tau_{oo})}{1-a\rho_{dd}}\right]E_s(t)/\pi \\ &+L_a(t) + \frac{aL_a(b)+(1-a)L_s}{1-a\rho_{dd}}(\tau_{do}+\tau_{oo}) \end{aligned} \quad (4)$$

Here, the first line on the right-hand side contains the solar-reflective part, and the second line the thermal contribution. This equation can be derived from Eqs. (1) and (2) by assuming a topographically flat, uniform Lambertian earth, with all surface reflectances equal to a. Although the 3 MODTRAN runs are made for a Lambertian surface, several distinct outputs are provided by the program, which allows us to derive atmospheric quantities that can be used next to model BRDF effects, topography effects, as well as adjacency effects for heterogeneous surfaces, by means of Eqs. (1) and (2). The most important MODTRAN outputs are listed in Table 4, where these are given by their MODTRAN name, their 4-letter name used in this paper, and the corresponding formula in the terminology of Eq. (4).

The total top-of-atmosphere radiance of Eq. (4) is equal to the sum of the terms PTEM, SFEM, PATH and GRFL in the middle column of Table 4, as can be verified by adding the corresponding expressions in the right column. Thanks to the fact that also the total transmittance TRAN and the direct solar contribution GSUN are provided in the MODTRAN output, one can derive all relevant atmospheric parameters, as will be shown later in this section.

Table 4
MODTRAN outputs, their names in this paper, and their formulas.

MODTRAN name	Our name	Formula
TOT_TRANS	TRAN	τ_{oo}
PTH_THRML	PTEM	$L_a(t) + \frac{aL_a(b)+(1-a)L_s}{1-a\rho_{dd}}\tau_{do}$
SURF_EMIS	SFEM	$(1-a)L_s\tau_{oo}$
SOL_SCAT	PATH	$\left[\rho_{so} + \frac{(\tau_{ss}+\tau_{sd})a\tau_{do}}{1-a\rho_{dd}}\right]E_s(t)/\pi$
GRND_RFLT	GRFL	$\frac{(\tau_{ss}+\tau_{sd})E_s(t)/\pi+L_a(b)+(1-a)L_s\rho_{dd}}{1-a\rho_{dd}}a\tau_{oo}$
DRCT_RFLT	GSUN	$a\tau_{ss}\tau_{oo}E_s(t)/\pi$

Fig. 5 illustrates the effect of the changes of albedo on the total TOA radiance output from MODTRAN for the spectral region 2000–14000 nm, in order to clearly show the transition area from the solar reflective to the thermal domain. Note that in the thermal domain (>8000 nm) an *increase* of the surface albedo gives a *decrease* of TOA radiances. This is due to the corresponding decrease of surface emissivity (Kirchhoff's law). In the region around 6000 nm the changes of surface albedo cause no change in the TOA radiances at all. This is due to the fact that in this region the atmospheric transmittance is zero, so that one observes only atmospheric spectral features.

The four separate terms PTEM, SFEM, PATH and GRFL for a surface albedo of 0.5 are illustrated for the same spectral range in Fig. 6. Here, a logarithmic scale was used on the Y-axis in order to accommodate the large dynamic range of the radiance values. Up to 4000 nm the term GRFL (ground-reflected contribution) dominates, whereas in the thermal domain SFEM and PTEM dominate, although GRFL remains important in this region.

From the previously defined components, one can also define the total ground contribution including surface emission as

$$\mathrm{GTOT} = \mathrm{GRFL} + \mathrm{SFEM},$$

and the total atmospheric contribution as

$$\mathrm{ATMO} = \mathrm{PATH} + \mathrm{PTEM}.$$

For these terms, one obtains in the four-stream terminology

$$\begin{aligned} \mathrm{GTOT} = \mathrm{GRFL} + \mathrm{SFEM} &= \frac{(\tau_{ss}+\tau_{sd})E_s(t)/\pi + L_a(b) + (1-a)L_s\rho_{dd}}{1-a\rho_{dd}}a\tau_{oo} + (1-a)L_s\tau_{oo} \\ &= \frac{(\tau_{ss}+\tau_{sd})aE_s(t)/\pi + aL_a(b) + (1-a)L_s}{1-a\rho_{dd}}\tau_{oo} \end{aligned}$$

$$\begin{aligned} \mathrm{ATMO} = \mathrm{PATH} + \mathrm{PTEM} &= \left[\rho_{so} + \frac{(\tau_{ss}+\tau_{sd})a\tau_{do}}{1-a\rho_{dd}}\right]E_s(t)/\pi + L_a(t) + \frac{aL_a(b)+(1-a)L_s}{1-a\rho_{dd}}\tau_{do} \\ &= \rho_{so}E_s(t)/\pi + L_a(t) + \frac{(\tau_{ss}+\tau_{sd})aE_s(t)/\pi + aL_a(b) + (1-a)L_s}{1-a\rho_{dd}}\tau_{do} \end{aligned}$$

In the following, albedos of 0, 0.5 and 1 are indicated by their percentages (0, 50 and 100) in order to be used as subscripts appended to the 4-letter radiometric MODTRAN quantities. One then obtains for GTOT, respectively,

$$\begin{aligned} \mathrm{GTOT}_0 &= L_s\tau_{oo} \\ \mathrm{GTOT}_{50} &= \frac{(\tau_{ss}+\tau_{sd})E_s(t)/\pi + L_a(b) + L_s}{2-\rho_{dd}}\tau_{oo} \\ \mathrm{GTOT}_{100} &= \frac{(\tau_{ss}+\tau_{sd})E_s(t)/\pi + L_a(b)}{1-\rho_{dd}}\tau_{oo} \end{aligned}.$$

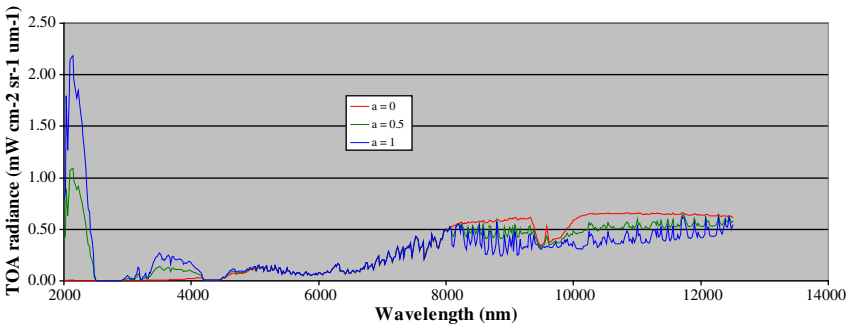

Fig. 5. Effect of changes in surface albedo on TOA radiances simulated with MODTRAN4 over the range 2000–14000 nm.

From the above equations, it can be verified that the differences

$$\Delta GTOT_{100} = GTOT_{100} - GTOT_0 \text{ and } \Delta GTOT_{50} = GTOT_{50} - GTOT_0$$

are related by the equations

$$(1-\rho_{dd})\Delta GTOT_{100} = (2-\rho_{dd})\Delta GTOT_{50} \\ = [(\tau_{ss}+\tau_{sd})E_s(t)/\pi + L_a(b) - (1-\rho_{dd})L_s]\tau_{oo}.$$

From the first identity it follows that the spherical albedo of the atmosphere is given by

$$\rho_{dd} = \frac{\Delta GTOT_{100} - 2\times\Delta GTOT_{50}}{\Delta GTOT_{100} - \Delta GTOT_{50}}.$$

For the difference between ATMO at 100% and 0% albedo one obtains

$$(1-\rho_{dd})\Delta ATMO_{100} = [(\tau_{ss}+\tau_{sd})E_s(t)/\pi + L_a(b) - (1-\rho_{dd})L_s]\tau_{do}.$$

Comparing this to the result of $\Delta GTOT_{100}$ leads to the conclusion that

$$\frac{\Delta ATMO_{100}}{\Delta GTOT_{100}} = \frac{\tau_{do}}{\tau_{oo}}, \text{ so that } \tau_{do} = \frac{\Delta ATMO_{100}}{\Delta GTOT_{100}}\tau_{oo} = \frac{\Delta ATMO_{100}}{\Delta GTOT_{100}} \times TRAN.$$

For the contributions PATH and PTEM one obtains for the differences between 100% and 0% albedo:

$$\Delta PATH_{100} = PATH_{100} - PATH_0 = \left[\frac{(\tau_{ss}+\tau_{sd})E_s(t)/\pi}{1-\rho_{dd}}\right]\tau_{do},$$

and

$$\Delta PTEM_{100} = PTEM_{100} - PTEM_0 = \left[\frac{L_a(b)}{1-\rho_{dd}} - L_s\right]\tau_{do} \\ = \frac{L_a(b) - (1-\rho_{dd})L_s}{1-\rho_{dd}}\tau_{do}.$$

Writing for the "optical term" $O = (\tau_{ss}+\tau_{sd})E_s(t)/\pi$, and for the "thermal term" $T = L_a(b) - (1-\rho_{dd})L_s$, one can summarize the previous results by:

$$(1-\rho_{dd})\Delta GTOT_{100} = (O+T)\tau_{oo} \\ (1-\rho_{dd})\Delta PATH_{100} = O\tau_{do} \\ (1-\rho_{dd})\Delta PTEM_{100} = T\tau_{do} \\ (1-\rho_{dd})\Delta ATMO_{100} = (O+T)\tau_{do}$$

It should be emphasized here that the MODTRAN outputs are always average radiances over certain spectral intervals. If there are large spectral variations within such an interval, then the average value of a product of spectral variables will not be equal to the product of their spectral averages over the interval, unless they are totally uncorrelated. However, high positive correlations are very likely, since these are mostly associated with a common cause, namely absorption lines from gasses in the atmosphere. In that case the average of a product will be greater than the product of the averages. Therefore, it is more correct to work with the gain factors as defined in the previous section than with products of averaged transmittances. It is for the same reason that in the following derivations $\approx$ is sometimes used instead of the equals sign, since the corresponding "equalities" are only approximately correct.

Since $\frac{O}{O+T} \approx \frac{O\tau_{do}}{O\tau_{do}+T\tau_{do}} = \frac{\Delta PATH_{100}}{\Delta ATMO_{100}}$, the terms $O\tau_{oo}$ and $T\tau_{oo}$ can be estimated from

$$O\tau_{oo} \approx \frac{O}{O+T}(O+T)\tau_{oo} = \frac{\Delta PATH_{100}}{\Delta ATMO_{100}}(1-\rho_{dd})\Delta GTOT_{100},$$

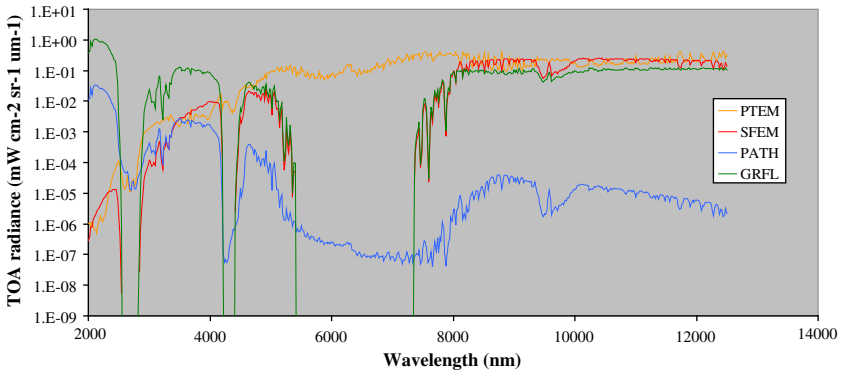

Fig. 6. TOA radiance contributions PTEM, SFEM, PATH and GRFL for a surface albedo of 0.5.

and

$$T\tau_{oo} \approx \frac{T}{O+T}(O+T)\tau_{oo} = \frac{\Delta PTEM_{100}}{\Delta ATMO_{100}}(1-\rho_{dd})\Delta GTOT_{100}.$$

Using $GSUN = a\tau_{ss}\tau_{oo}E_s(t)/\pi$, the sky radiance term of solar origin can be estimated from $O\tau_{oo} = (\tau_{ss}+\tau_{sd})\tau_{oo}E_s(t)/\pi$ by subtracting the direct solar contribution at 100% albedo, or

$$\tau_{sd}\tau_{oo}E_s(t)/\pi = O\tau_{oo} - GSUN_{100}.$$

This term is also known as G_{sdoo} (see previous section). The term G_{ssoo} turns out to be equal to $GSUN_{100}$.

The term G_{sddo} is derived from G_{sdoo} by multiplication with the ratio $\frac{\tau_{do}}{\tau_{oo}} = \frac{\Delta ATMO_{100}}{\Delta GTOT_{100}}$.

The term G_{mult} is found by multiplication of $GSUN_{100}$ with ρ_{dd}.

From the term $T\tau_{oo} = L_a(b)\tau_{oo} - (1-\rho_{dd})L_s\tau_{oo}$ one can isolate the term $L_s\tau_{oo} = SFEM_0$, so that

$$L_a(b)\tau_{oo} = T\tau_{oo} + (1-\rho_{dd})SFEM_0,$$

and one obtains

$$L_a(b) = [T\tau_{oo} + (1-\rho_{dd})SFEM_0]/TRAN.$$

For PTEM at 0% albedo one finally obtains

$$PTEM_0 = L_s\tau_{do} + L_a(t),$$

or

$$L_a(t) = PTEM_0 - \frac{\Delta ATMO_{100}}{\Delta GTOT_{100}}SFEM_0.$$

The technical details of the MIT including thermal domain radiation have now been exemplified. The final output consists of 11 spectral variables by means of which one can describe in a unified way the surface–atmosphere interaction over the solar-reflective and thermal domains, thereby including BRDF effects and even directional emissivity.

3.3. Wide-swath imagery modeling

For the modeling of wide swath images such as for the Sentinel-3 sensors, the MODTRAN outputs have to be interpolated over the sun-target-sensor angular geometry specified by the solar zenith angle SZA, the viewing zenith angle VZA and the relative azimuth angle RAA. In order to enable this interpolation, look-up tables were generated with 5 degree intervals in both zenith angles, and 45 degree intervals in RAA. The ranges covered were 0–55° for VZA, 0–70° for SZA and 0–180° for RAA. The wider interval used in the case of RAA is possible because the dependence of the path radiance on RAA can be described accurately by a cosine series of 5 terms. For the combination of the zenith angles SZA and VZA a bilinear interpolation is applied. Surface bidirectional reflectance modeling by the SLC model is very fast, so in this case the model can be called pixel by pixel. This is also done to accommodate textural variations over the image.

3.4. Spectral properties of the OLCI and SLSTR sensors

In order to create flexibility in the simulation of various instrument spectral response functions, the concept of so-called microbands is applied. Microbands have been defined in such a way that all spectral bands of the given sensors are covered and that small additional spectral shifts are still allowed to study their impact. In this way it is possible to obtain realistically simulated sensor responses for any instrument by a weighted summation of the responses in the microbands. Table 5 gives a summary of the spectral bands of the SLSTR and OLCI instruments and the connected definition of ranges of microbands.

4. Examples

4.1. Local topography effects

In order to illustrate the effect of topography on the scene simulation a test case in the Alps was selected. The simulation results are illustrated by different stages: first (Fig. 7a) at Bottom of Atmosphere (BOA) level, showing the calculated directional reflectances. These were simulated based on textural fields listed in Table 2, which have been derived from an input LANDSAT TM image through SLC model inversion. The second step (Fig. 7b) is after applying the MODTRAN Interrogation Technique and considering the local illumination effects. Here at TOA (Top of Atmosphere) level the topography results in local effects, e.g. lower radiances at North facing hill slopes. Fig. 7c shows the simulated TOA radiances for the thermal band. The cooler North facing hills are here caused by lower surface temperatures. The band selection of the color illustrations (SWIR, NIR, red in RGB) allows representing the 3 main spectral ranges in the reflective part of the spectrum. The area displayed covers an area of 70 km by 70 km South of Munich with elevation differences of 2500 m and a pixel resolution of 100 m. The simulated BOA reflectances are free from any terrain influences, as can be expected. When modeling the radiances reaching the sensor (TOA) the illumination effect plays a dominant role. At TOA radiance level the simulated image compares very well with the observed one (Fig. 7d). The atmospheric visibility for this scene was very high and estimated at 80 km in the forward simulation.

Since satellite data for Sentinel-3 are not available for validation purposes, it was analyzed how well the simulation exercise can reproduce the input TM image that was used for the retrieval of textural information. For validation, Fig. 8 shows a scatter plot of simulated versus measured radiances for the Alpine scene illustrated in Fig. 7. The spectral bands were those of Fig. 7 (SWIR, NIR and red). A number of 4900 pixels were selected randomly. A fair agreement between

Table 5
Selection of spectral resolution of the microbands used in the LSG in order to allow a flexible handling of the spectral response functions for OLCI (21 bands between 0.4 and 1.04 μm with spectral resolutions varying between 3.75 and 40 nm) and SLSTR, which spectral bands are listed in the table.

Covered SLSTR bands	Center wavelength [μm]	Spectral Width [μm]	Starting band [μm]	Ending band [μm]	Spectral resolution [μm]	Number of microbands
	0.555					
1–3	0.659	0.020	0.38	1.05	0.00125	537
	0.865					
4	1.375	0.015	1.360	1.390	0.00125	25
5	1.610	0.060	1.550	1.670	0.00500	25
6	2.250	0.050	2.200	2.300	0.00500	21
7	3.740	0.380	3.360	4.110	0.02500	31
8–9	10.850	0.900	9.950	11.750		
	12.000	1.000	11.000	13.000	0.05000	62

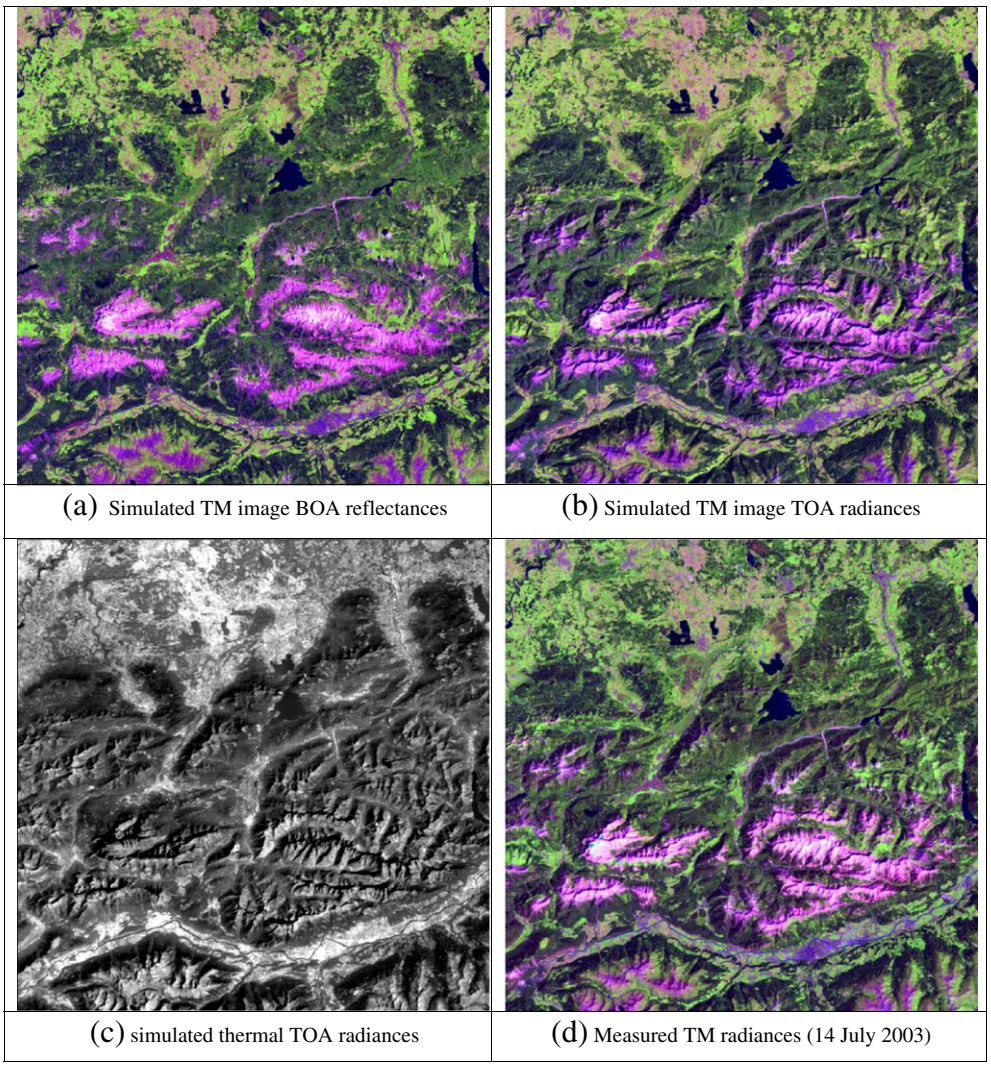

Fig. 7. Graphical illustration of simulation results for a mountainous region in the Alps (blue = 665 nm, green = 835 nm, red = 1.7 μm in (a), (b) and (d); 11.5 μm in (c)). (d) shows the input TM image with identical look-up-table as the corresponding simulation results in (b).

simulation and measurements was obtained for all three spectral ranges. The overall RMS error for the radiance values amounts to 6.1 W/(m² sr μm).

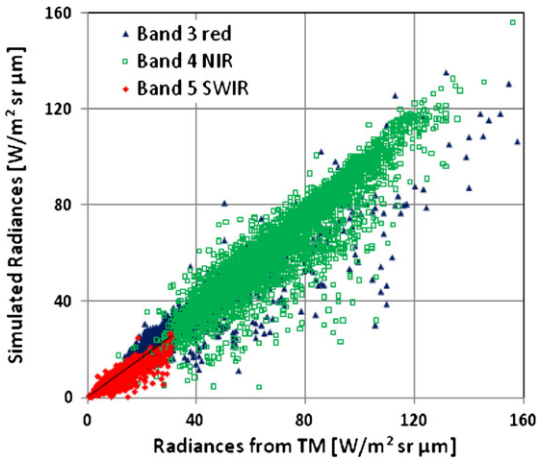

Fig. 8. Validation plot of simulated versus measured radiances for the Alpine scene illustrated in Fig. 7.

4.2. Wide-swath BRDF effects

In wide-swath remote sensing imagery both the local viewing angles (zenith and azimuth) and the solar angles (zenith and azimuth) change substantially over an image. BRDF effects and atmospheric influences are a function of the solar and viewing zenith angles (SZA and VZA) and of the relative azimuth angle, which is defined as the absolute difference in both azimuth angles (SAA and VAA), ranging from 0 to 180°. If both azimuth directions are given in degrees from local North (range 0–360°), then the relative azimuth angle can be calculated by the formula

$$RAA = 180 - |180 - |(SAA - VAA)||.$$

Fig. 9 (top) illustrates how the angles SZA (left) and VZA (middle) vary over an image for the OLCI instrument, and RAA (right) for the SLSTR instrument over South Sweden under summer conditions (21st June). The angular effects have been amplified in order to cover the whole realistic range occurring in Sentinel-3 scenes, although in reality the geographic extent of the image of Southern Sweden just covers 20% of a OLCI scene. In Fig. 9 (bottom) the corresponding BRDF effects are illustrated by showing the bidirectional surface reflectance r_{so} in the green, red and near infrared for OLCI and the conical

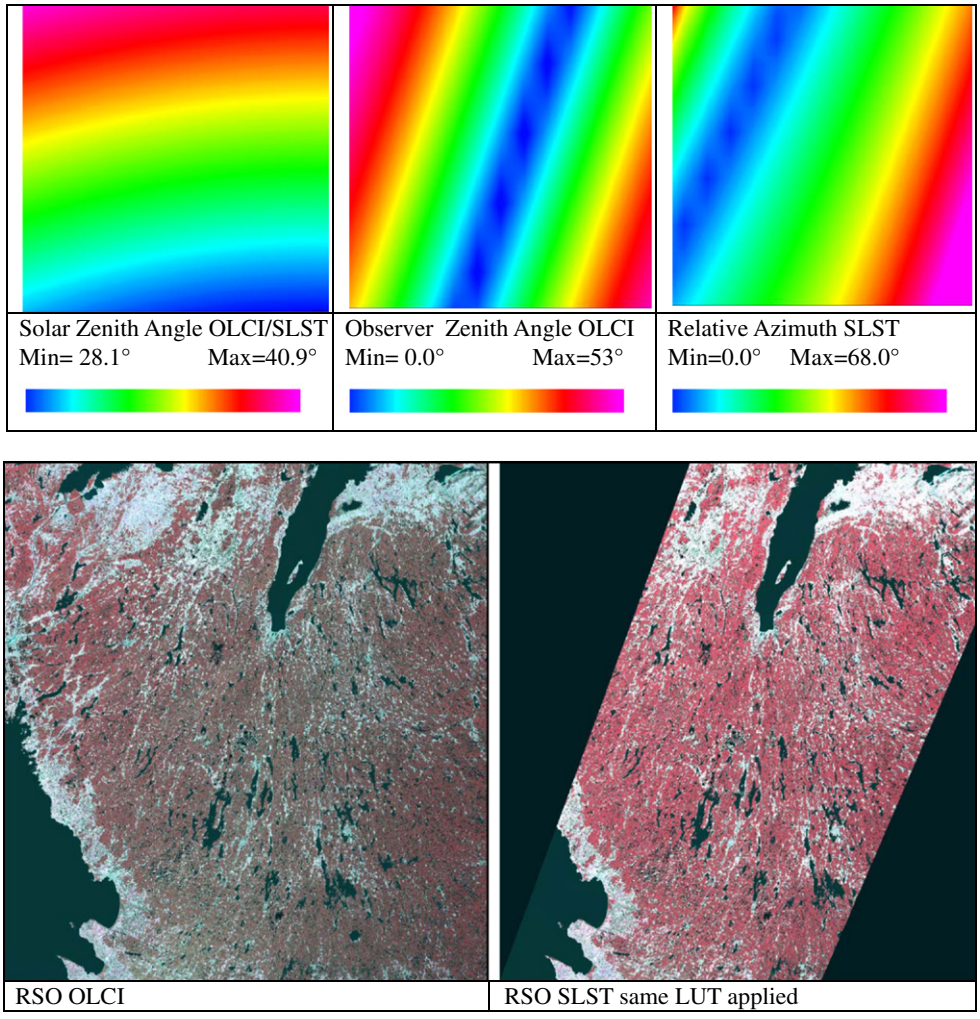

Fig. 9. Example of a simulated OLCI and SLST wide swath image (bottom, RGB = 680 nm, 555 nm, 455 nm) showing BRDF and solar illumination effects. The angular variations illustrated in the top of Fig. 9 are in realistic ranges for the Sentinel-3 instruments but have been amplified by a factor of 5 compared to the geographic extent of the scene to exaggerate the effects. Effects for OLCI (left) and SLSTR (right). The angular variations are representative for these sensors.

backward-looking scanner SLSTR, which has a narrower swath. This illustrates the large BRDF effect of backward looking under 55° compared to the across-track looking of OLCI. In both cases the same color look-up table was applied, so that the observed differences are really due to the different scanning configurations.

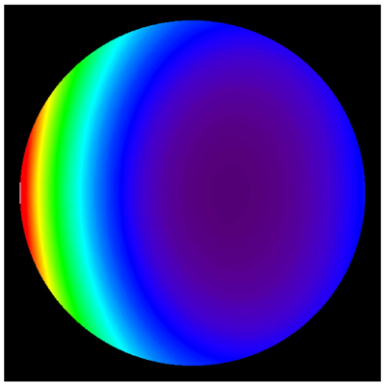

Fig. 10. Polar plot of the TOA radiance at 550 nm for a visibility of 20 km and a solar zenith angle of 45° to illustrate the smoothness of the angular interpolation procedure.

4.3. Angular interpolation of atmospheric effects

To test the smoothness of all the angular interpolations, a test image was generated by creating a polar plot of the TOA radiance for viewing zenith angles up to 60°, and a relative azimuth comprising the full circle from −180 to 180°. This plot was made for a visibility of 20 km, a solar zenith angle of 45°, a wavelength of 550 nm, and a surface albedo of 0.25. In this way all interpolated quantities have a chance of playing a role, with a maximum chance of discovering errors in one or more interpolated MIT parameters. The result is displayed via a rainbow color look-up table in Fig. 10. It appears that this picture looks perfectly smooth, so the angular interpolation method was found to function adequately.

5. Discussion and conclusion

In this paper we have shown that image simulation of Sentinel-3 data for the sensors OLCI and SLSTR is feasible by combining radiative transfer models for soil–vegetation objects and water bodies with outputs from an atmospheric model like MODTRAN. Case studies illustrate simulated scenes and a comparison with a real case gave confidence of the model approach. The presented simulator has however its limitations. Since it is concentrating on the radiative transfer part

of a land scene generator, sensor-specific effects like spectral response function of the individual bands, digitization, sensor noise, smile effect, geometric resolutions and point spread function of the different sensors are not considered in this study. Instead, oversampling in the spectral and spatial domains is provided by the simulation tool in order to allow later resampling to the actual sensor characteristics which may vary during the construction of a sensor. Thus also different specifications of a sensor can be tested.

However, image simulation is not only useful to get familiar with future satellite missions, and to test advanced algorithms for the retrieval of surface and atmosphere properties, but it can also be applied in multi-sensor approaches in which the image modeling functions as a bridge between the various types of sensors and satellite missions. Confronting simulated images with actual data from various sensor systems on board of multiple satellites enables a continuous updating of surface properties by a feedback mechanism which tries to match the simulated TOA radiance data with the corresponding satellite observations. This is done by adjusting the surface properties on the basis of the differences between simulations and observations. As an example, take a very important surface property of vegetation, its leaf area index, LAI. Nearly continuous time series of LAI could be obtained by combining the data from several satellite missions in a data assimilation approach in which modeled and real observations of TOA radiances would be compared. This would lead to true multi-sensor products as alternatives for well-known sensor-specific products like MODIS-LAI. The simulation methodology as discussed for the Sentinel-3 sensors can be applied to any other sensor operating in the solar-reflective or thermal domain, which means that for all those sensors corresponding simulated images could be generated, and that they so could contribute to a consistent line of multi-sensor land surface property products.

Acknowledgment

In the frame of Sentinel-3 phases B to E, an Optical System Performance Simulator is under development by Thales Alenia Space — France for the European Space Agency. As part of this simulator the "Sentinel-3 Land Scene Generator" was subcontracted to VISTA and ITC under contract no. 15550001256. Thanks to Sandrine Mathieu (TAS-F) and Helge Rebhan (ESA ESTEC) for managing this study. Many thanks to Silke Migdall (VISTA) for processing the Landsat images and for retrieving the textural files. NASA/USGS is thanked for providing the Landsat imagery. The authors would further like to thank Peter Gege of DLR, Germany, for providing the water optical model WASI.

Finally we would like to express our thanks to three anonymous reviewers for their constructive comments, from which the final version of the paper has greatly benefited.

References

Bach, H., & Mauser, W. (1994). Modelling and model verification of the spectral reflectance of soils under varying moisture conditions. *Proc. IGARSS'94 symposium, Pasadena, Vol. 4.* (pp. 2354–2356).

Berk, A., Anderson, G. P., Acharya, P. K., Chetwynd, J. H., Hoke, M. L., Bernstein, L. S., et al. (1999). *MODTRAN4 version 2 user's manual, Air Force Research Laboratory, Space Vehicles Directorate, Hanscom AFB, MA, USA.*

Gascon, F., Gastellu-Etchegorry, J. P., & Lefèvre, M. J. (2001). Radiative transfer model for simulating high-resolution satellite images. *IEEE Transactions on Geoscience and Remote Sensing*, *39*(9), 1922–1926.

Gastellu-Etchegorry, J. P., Martin, E., & Gascon, F. (2004). DART: A 3-D model for simulating satellite images and surface radiation budget. *International Journal of Remote Sensing*, *25*(1), 75–96.

Gege, P. (2004). The Water Color Simulator WASI: An integrating software tool for analysis and simulation of optical in situ spectra. *Computers & Geosciences*, *30*(5), 523–532.

Gege, P. (2005). The Water Colour Simulator WASI — User manual for version 3., DLR-IB 564-1/2005, 83 pages. http://elib.dlr.de/19338/

Hapke, B. W. (1981). Bi-directional reflectance spectroscopy 1. Theory. *Journal of Geophysical Research*, *86*, 3039–3054.

Jacquemoud, S., & Baret, F. (1990). PROSPECT: A model of leaf optical properties spectra. *Remote Sensing of Environment*, *34*, 75–91.

Pinty, B., Verstraete, M. M., & Dickinson, R. E. (1989). A physical model for predicting bi-directional reflectances over bare soil. *Remote Sensing of Environment*, *27*, 273–288.

Poglio, T., Mathieu-Marni, S., Ranchin, T., Savaria, E., & Wald, L. (2006). OSiRIS: A physically based simulation tool to improve training in thermal infrared remote sensing over urban areas at high spatial resolution. *Remote Sensing of Environment*, *104*, 238–246.

Verhoef, W. (1984). Light scattering by leaf layers with application to canopy reflectance modeling: The SAIL model. *Remote Sensing of Environment*, *16*, 125–141.

Verhoef, W. (1998). Theory of radiative transfer models applied in optical remote sensing of vegetation canopies, PhD Thesis, Wageningen Agricultural University, 310 pp.

Verhoef, W., & Bach, H. (2003). Simulation of hyperspectral and directional radiance images using coupled biophysical and atmospheric RT-models. *Remote Sensing of Environment*, *87*, 23–41.

Verhoef, W., & Bach, H. (2007). Coupled soil–leaf–canopy and atmosphere radiative transfer modeling to simulate hyperspectral multi-angular surface reflectance and TOA radiance data. *Remote Sensing of Environment*, *109*(2), 166–182.

Widlowski, J. L., Taberner, M., Pinty, B., Bruniquel-Pinel, V., Disney, M., Fernandes, R., et al. (2007). Third radiation transfer model intercomparison (RAMI) exercise: Documenting progress in canopy reflectance models. *Journal of Geophysical Research*, *112*, D09111 112, D Atmospheres.